Journal of Ship Research, Vol. 50, No. 3, September 2006, pp. 259–267

A Note on the Development of a Nonlinear Axisymmetric Reentrant Jet Cavitation Model

James S. Uhlman

Engineering Technology Center, Alion Science and Technology Corporation, Middletown, Rhode Island, USA

The boundary integral method is formulated for the problem of the fully nonlinear, axisymmetric potential flow past a body of revolution. A model is devised for the exact formulation of the reentrant jet cavity closure condition. It is demonstrated that the solution obtained is essentially independent of the length selected for the jet. Results obtained using the reentrant jet cavity closure model are compared with those obtained using the Riabouchinsky-type cavity closure model used by Uhlman (1987, 1989) and with experimental results. The agreement between the two cavity closure models is seen to be excellent, with the Riabouchinsky wall results deviating only slightly at short cavity lengths. The agreement of the reentrant jet model with the experimental data is also excellent, although the addition of the viscous component of drag is seen to be required for cavitating cones of sufficiently small half-angle.

1. Introduction

THE MODELING of the cavitating flow about various bodies has been the subject of much research. The early work approached the problem from the analytical theory of free streamlines and, although exact, was limited to two-dimensional problems (see, e.g., Efros 1946, Gilbarg & Serrin 1950, Gilbarg 1960). The focus then shifted to the linear theory of the flow about hydrofoils undergoing both partial and supercavitation (see, e.g., Tulin 1953, 1964, Guerst 1959, 1960, Leehey 1973, Uhlman 1978). The advent of high-speed computing brought about the development of numerical approaches to the analysis of both linear and nonlinear models of cavitation phenomena. These efforts were, again, largely directed to the analysis of lifting surface flows (see, e.g., Pellone & Rowe 1981, Uhlman 1983, 1987, 1989, Fine 1992, Kinnas & Fine 1993, Fine & Kinnas 1993, Dang & Kuiper 1999a, 1999b, Krishnaswarmy et al. 2001). Efforts aimed at the prediction of the flow about nonlifting bodies received much less attention. Notable exceptions are Tulin (1953), Brennen (1969), and Chou (1974). More recently, axisymmetric flows have also been addressed by Uhlman et al. (1998).

Manuscript received at SNAME headquarters October 2002; revised manuscript received March 2005.

Interestingly, of all these efforts, only the early work of Efros (1946), Gilbarg (1960), and the more recent work of Uhlman et al. (1998), Dang and Kuiper (1999a, 1999b), and Krishnaswarmy et al. (2001) have employed the correct, physical, reentrant jet model for the cavity termination. All of the other approaches employed some method to "close" the cavity (albeit occasionally with nonzero net flux). The linear theories typically imposed a condition specifying the net source strength. The nonlinear approaches of Pellone and Rowe (1981), Fine (1992), and Kinnas and Fine (1993) employed similar conditions, while Uhlman (1983, 1987, 1989) implemented a modified Riabouchinsky wall at the end of the cavity to close the cavity.

Most of these approaches typically resulted in solutions with zero net source strength. The exact reentrant jet models of Efros (1946), Gilbarg (1960), Uhlman et al. (1998), and Dang and Kuiper (1999a, 1999b), however, yield a negative net source strength by effectively directing the reentrant jet across a branch cut and onto another Riemann sheet. While the work of Krishnaswarmy et al. (2001) also employs such a reentrant jet, they insert an artificial source into the flow field, which balances the mass flux through the reentrant jet. The present work is an extension of the work of Uhlman et al. (1998). It employs methods quite similar to those of Dang and Kuiper (1999a, 1999b) and Krishnaswarmy et al. (2001), although without the source employed in the latter.

2. Mathematical formulation

Following the work of Fine (1992), Kinnas and Fine (1993), and Fine and Kinnas (1993), a potential-based model of the cavitating flow is employed. The basis for the potential flow model to be presented here is Green's third identity applied to the axisymmetric disturbance velocity potential; that is,

$$\beta\varphi(r,\theta) = \iint_S \left\{ \frac{\partial\varphi(\rho,\varphi)}{\partial n} G(r,\theta;\rho,\varphi) - \varphi(\rho,\varphi)\frac{\partial G(r,\theta;\rho,\varphi)}{\partial n} \right\} \rho d\varphi ds \tag{1}$$

where the normal is directed out of the fluid, s is arclength along a meridian,

$$\beta = \begin{cases} 4\pi, \text{ in } V \\ 2\pi, \text{ on } S \\ 0, \text{ in } V^c \end{cases} \tag{2}$$

and the total and disturbance potentials are related by

$$\Phi = x + \varphi \tag{3}$$

where all quantities have been made dimensionless with respect to ρ, U_∞, and d.

The boundary conditions to be applied are

$$\frac{\partial\Phi}{\partial n} = 0, \qquad \text{on } S_b \cup S_c \tag{4}$$

and

$$\frac{\partial\Phi}{\partial s} = \sqrt{1+\sigma}, \qquad \text{on } S_c \tag{5}$$

or equivalently

$$\frac{\partial\varphi}{\partial n} = -n_x, \qquad \text{on } S_b \cup S_c \tag{6}$$

and

$$\frac{\partial\varphi}{\partial s} = \sqrt{1+\sigma} - s_x, \qquad \text{on } S_c \tag{7}$$

where $\mathbf{n}$ and $\mathbf{s}$ are unit vectors normal and tangent to the body/cavity boundary, respectively, and the various boundary segments are shown in Fig. 1. The last boundary condition may be integrated to yield

$$\varphi = \varphi_0 + \sqrt{1+\sigma}\,(s - s_0) - (x - x_0), \qquad \text{on } S_c \tag{8}$$

where φ_0 is the potential at the detachment point of the cavity on the body.

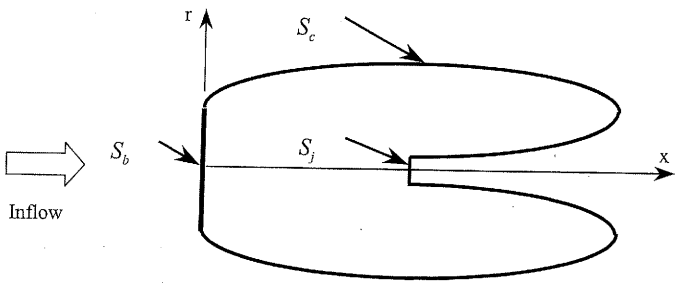

Fig. 1 Problem geometry and boundary designations

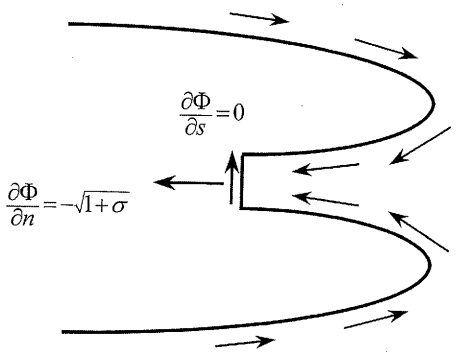

Fig. 2 Illustration of conditions satisfied on the cross section of the reentrant jet

3. Jet conditions

The cavity boundary conditions hold right up to where the reentrant jet is crossed by the integration boundary. It is assumed that the jet has asymptoted to a constant diameter and a constant velocity throughout its cross section. The conditions at the jet cross section are then that the velocity normal to the cross section is the same as that at the cavity wall and that the potential at the cross section is constant and equal to that at the edge of the jet cross section. On the cross section of the reentrant jet, the conditions are then

$$\frac{\partial\varphi}{\partial n} = \sqrt{1+\sigma} - n_x, \qquad \text{on } S_j \tag{9}$$

and

$$\varphi = \varphi_0 + \sqrt{1+\sigma}\,(s_j - s_0) - (x_j - x_0), \qquad \text{on } S_j \tag{10}$$

where s_j and x_j are the arclength and the x coordinate at the edge of the jet cross section, respectively (Fig. 2).

Nomenclature

Φ = total velocity potential
φ = disturbance velocity potential
$\mathbf{n}$ = normal vector
$\mathbf{s}$ = tangent vector
σ = cavitation number, $= \dfrac{p - p_c}{\frac{1}{2}\rho U_\infty^2}$
G = Green's function
U_∞ = freestream speed
s = arclength in meridional plane
$\mathbf{x}$ = field point location
ξ = source point location or integration variable
ρ = fluid density
d = cavitator diameter
C_d = drag coefficient, $= \dfrac{D}{\frac{1}{2}\rho U_\infty^2 \frac{\pi}{4} d^2}$
p_c = cavity pressure

4. Governing integral equations

Placing the unknowns on the left-hand side and the knowns on the right-hand side of the equation, we find that Green's third identity becomes

$$2\pi\varphi + \iint_{S_b} \varphi \frac{\partial G}{\partial n} dS - \iint_{S_c} \frac{\partial \varphi}{\partial n} G dS = \iint_{S_b+S_j} \frac{\partial \varphi}{\partial n} G dS - \iint_{S_c+S_j} \varphi \frac{\partial G}{\partial n} dS \tag{11}$$

on the wetted portion of the body/cavity boundary and

$$\iint_{S_b} \varphi \frac{\partial G}{\partial n} dS - \iint_{S_c} \frac{\partial \varphi}{\partial n} G dS = \iint_{S_b+S_j} \frac{\partial \varphi}{\partial n} G dS - 2\pi\varphi - \iint_{S_b+S_j} \varphi \frac{\partial G}{\partial n} dS \tag{12}$$

on the cavity boundary. Implementing the above boundary conditions, we find that equation (11) becomes

$$\begin{aligned} 2\pi\varphi &+ \iint_{S_b} \varphi \frac{\partial G}{\partial n} dS - \iint_{S_c} \frac{\partial \varphi}{\partial n} G dS + \varphi_0 \iint_{S_c+S_j} \frac{\partial G}{\partial n} dS \\ &+ \sqrt{1+\sigma}\left[\iint_{S_c+S_j} (s - s_0) \frac{\partial G}{\partial n} dS - \iint_{S_j} G dS \right] \\ &= -\iint_{S_b} n_x G dS - \iint_{S_j} n_x G dS + \int\int_{S_c+S_j} (x - x_0) \frac{\partial G}{\partial n} dS \end{aligned} \tag{13}$$

on the body and equation (12) becomes

$$\begin{aligned} &\iint_{S_b} \varphi \frac{\partial G}{\partial n} dS - \iint_{S_c} \frac{\partial \varphi}{\partial n} G dS + \varphi_0 \left[2\pi + \iint_{S_c+S_j} \frac{\partial G}{\partial n} dS \right] \\ &+ \sqrt{1+\sigma}\left[2\pi (s - s_0) + \iint_{S_c+S_j} (s - s_0) \frac{\partial G}{\partial n} dS - \iint_{S_j} G dS \right] \\ &= -\iint_{S_b} n_x G dS - \iint_{S_j} n_x G dS + \left[2\pi (x - x_0) + \int\int_{S_c+S_j} (x - x_0) \frac{\partial G}{\partial n} dS \right] \end{aligned} \tag{14}$$

on the cavity boundary.

In addition to these equations, an auxiliary condition is required. Here we impose the condition that the net source strength is equal to the flux through the jet, which may be expressed as

$$\iint_{S_b+S_c+S_j} \frac{\partial \varphi}{\partial n} dS = \sqrt{1+\sigma} \iint_{S_j} dS \tag{15}$$

or equivalently

$$\iint_{S_c} \frac{\partial \varphi}{\partial n} dS = \iint_{S_b} n_x dS + \iint_{S_j} n_x dS \tag{16}$$

Computation of the axisymmetric Green functions is addressed in Appendices A and B.

5. Numerical aspects

To obtain the solution to these equations, they are discretized into flat panels with piecewise constant source and normal dipole distributions. The cavity length and initial shape are specified and the equations are solved for the unknown values of the potential on the body, the unknown values of the normal velocity on the cavity, and the quantity $\sqrt{1+\sigma}$, from which the cavitation number can be obtained. The kinematic boundary condition on the cavity is then employed to update the shape of the cavity boundary, while maintaining constant cavity length. The solution is then obtained using this new cavity shape, and this procedure is repeated until convergence has been achieved (Fig. 3).

The initial cavity shape is composed of straight lines that join together to give the specified cavity length and jet length. An example for a flat disk cavitator is presented in Fig. 4. The cavity shape is updated between iterations by computing the velocities induced at the center of each panel and rotating the panels such that they are parallel to that velocity starting at the point of detachment of the cavity from the cavitator. Specifically, if the old position of a panel endpoint relative to its upstream end is given by $(\Delta x, \Delta y)$, then the new position of the panel endpoint is assumed to be given by $(\Delta x + \delta x, \Delta y + \delta y)$. The kinematic boundary condition then requires that

$$\frac{\Delta y + \delta y}{\Delta x + \delta x} = \tan(\theta + \delta\theta) = \frac{v}{u} \tag{17}$$

where the geometric quantities are illustrated in Fig. 4. Assuming rotation of the panel, the new displacements of its endpoints are readily shown to be given by

$$\begin{aligned} \delta x &= -\Delta y \, \delta\theta \\ \delta y &= \Delta x \, \delta\theta \end{aligned} \tag{18}$$

for small rotations, where

$$\delta\theta = \frac{v\Delta x - u\Delta y}{u\Delta x + v\Delta y} \tag{19}$$

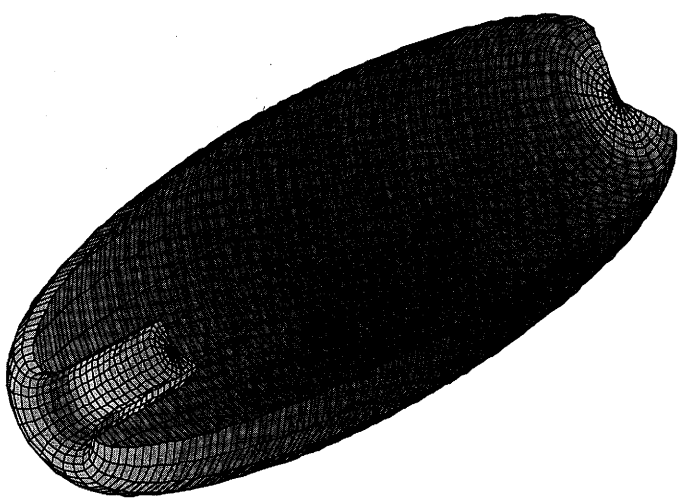

Fig. 3 Cut-away view of an axisymmetric cavity with a reentrant jet behind a disk cavitator with $l/d = 5$. Shades represent the disturbance potential. Solution has been revolved about the axis of symmetry to obtain cut-away view.

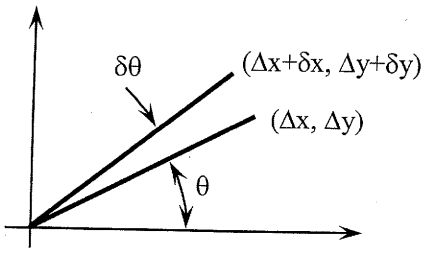

Fig. 4 Geometry for panel alignment

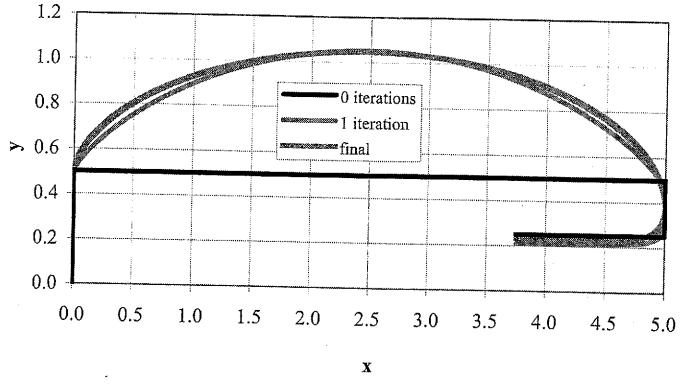

Fig. 5 Initial cavity shape, cavity shape after first iteration, and final cavity shape

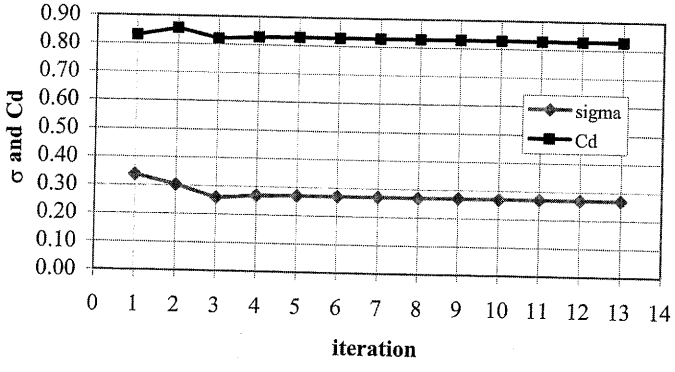

Fig. 6 Convergence with iteration number for a disk with $l_{cav}/d = 5.00$, $l_{jet}/d = 3.75$

These displacements, $(\delta x, \delta y)$, are computed at each panel endpoint starting at the upstream detachment point of the cavity and are then added to all panel endpoints downstream of the current panel. These displacements have the effect of altering the length of the cavity. To counter this, the cavity is then stretched in such a manner that the cavity length and jet length are returned to their original specified values. The initial cavity shape, cavity shape after the first iteration, and the final converged cavity shape are presented in Fig. 5. The solution is considered to have converged when the cavitation number and the drag coefficient have converged to some specified level of accuracy. The convergence of these quantities as a function of iteration number is presented in Fig. 6. The shape of the cavity can be shown to converge at roughly the same rate as these quantities. Convergence with number of panels is addressed in the next section.

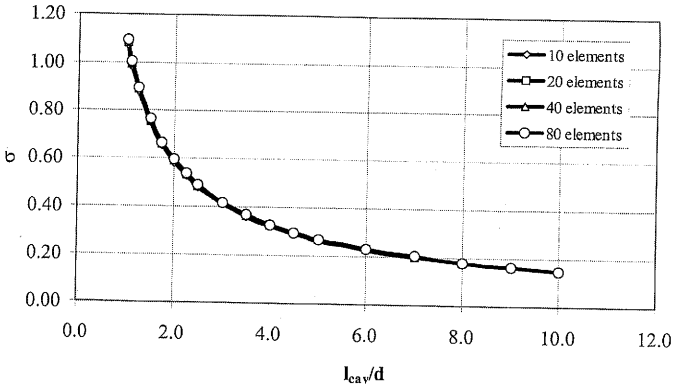

Fig. 7 Convergence of the cavitation number with increasing number of elements over the cavitator, $l_{jet}/d = 75\% l_{cav}/d$. (The number of elements over the cavity and the jet are proportional.)

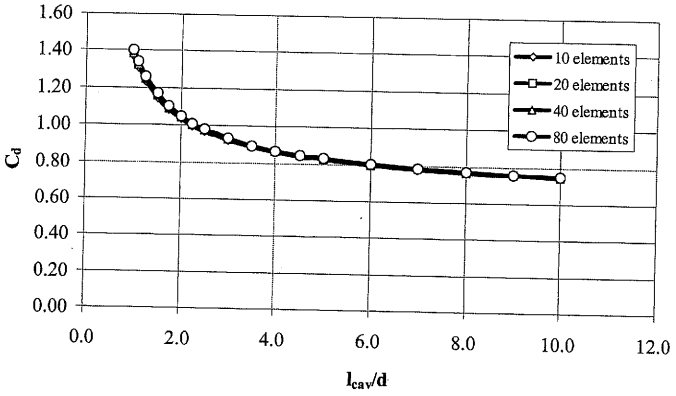

Fig. 8 Convergence of the drag coefficient with increasing number of elements over the cavitator, $l_{jet}/d = 75\% l_{cav}/d$

6. Results

The results presented herein are exact in the potential flow limit within discretization error. Upon convergence, the kinematic condition is satisfied on the cavitator and both the kinematic and dynamic conditions are satisfied on the cavity boundary. A typical solution is presented in Fig. 3, illustrating the cavity and jet shape obtained and the disturbance potential on the body/cavity boundary.

The convergence of the solution with increasing numbers of elements is presented in Figs. 7, 8, and 9. These figures show that, while the cavitation number and the drag coefficient computed for a given cavity length converge quite rapidly, the jet diameter converges somewhat more slowly. This is attributed to the fact that the cavitation number is a global quantity in the solution, while the jet diameter is a local quantity and is more dependent on the resolution of the cavity boundary.

The effect of the assumed jet length is presented in Fig. 10. It is readily seen that the shape of the cavity is essentially independent of the assumed jet length. The computed values of the cavitation number, jet diameter, and drag coefficient can be shown to be virtually independent of the jet length.

The dependence of the cavitation number on the cavity length is presented in Fig. 11. The results from the present reentrant jet

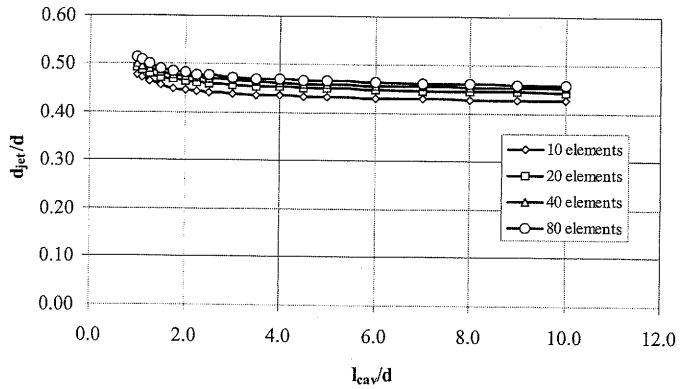

Fig. 9 Convergence of the jet diameter with increasing number of elements over the cavitator, $l_{jet}/d = 75\% l_{cav}/d$

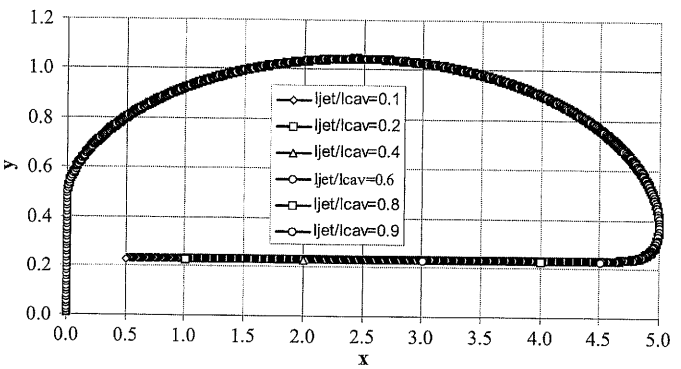

Fig. 10 Comparison of solutions for $l/d = 5$ for various values of the jet length

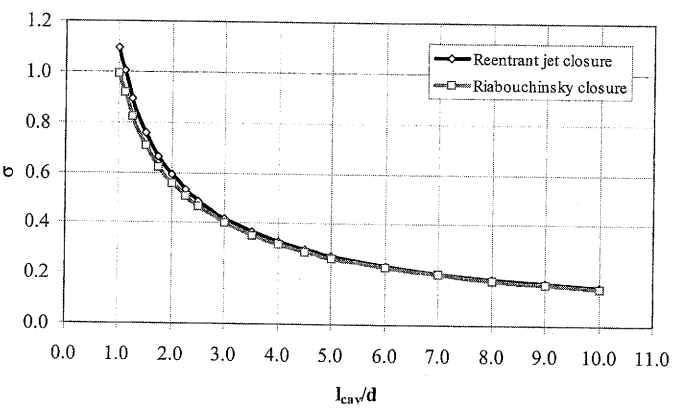

Fig. 11 Comparison of the dependence of cavitation number on cavity length as predicted using a reentrant jet cavity closure model and a Riabouchinsky-type cavity closure model

formulation and a Riabouchinsky wall formulation (see, e.g., Uhlman 1987, 1989, Uhlman et al. 1998) are shown. These results are in good agreement, particularly as the cavity length becomes large. At small cavity lengths it is seen that the Riabouchinsky wall formulation slightly underpredicts the cavitation number for a given cavity length. This effect is further explored in Fig. 12, which shows that for equal cavitation numbers the Riabouchinsky

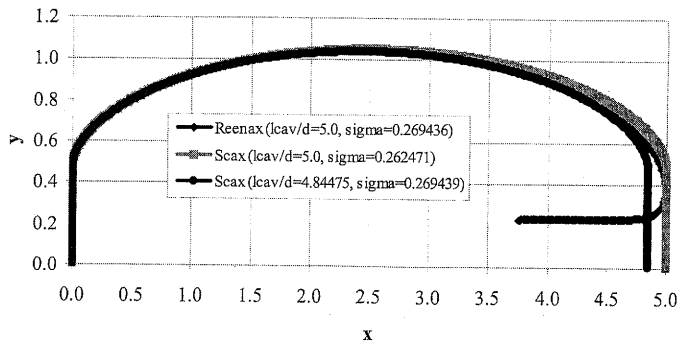

Fig. 12 Comparison of cavity shapes from the reentrant jet and Riabouchinsky wall formulations at equal cavity lengths and cavitation numbers

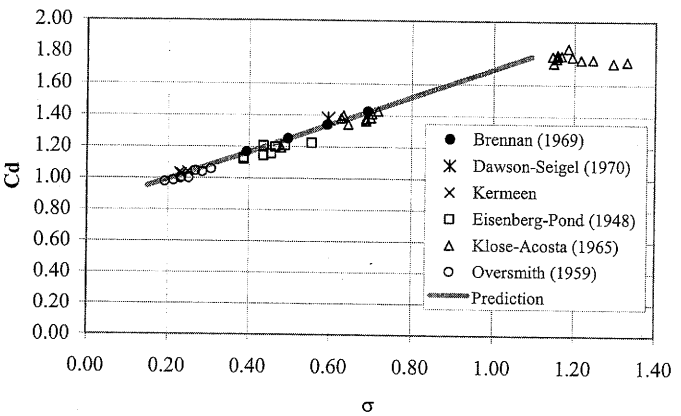

Fig. 13 Comparison of predicted and experimental drag coefficients for a disk cavitator for $1 \leq l_{cav}/d \leq 10$ (data from May 1975)

wall formulation predicts a slightly shorter cavity, and at equal cavity lengths the Riabouchinsky wall model predicts a cavity that is fuller at the aft end of the cavity.

Comparisons of the predicted and measured drag coefficients for a disk cavitator are presented in Figs. 13 and 14. The agreement is seen to be well within the scatter of the data, although leaning toward the high side for small cavitation numbers. Note that there can be no viscous component to the drag for a disk cavitator due to the fact that its tangent vector is always perpendicular to the drag direction. As a further consistency check, Fig. 15 presents a comparison of the drag computed by integration of the pressure over the disk cavitator with the drag predicted by a control volume analysis (see Appendix C). Again, the agreement is excellent.

Figure 16 presents a comparison of the predicted and measured drag on conical cavitators of 15 deg half-angle. In this case the viscous drag does contribute to the overall drag. Figure 16 shows two drag predictions: one for the inviscid case and one assuming laminar flow where the viscous drag is computed using Thwaites method (see, e.g., White 1974). The Reynolds numbers of the various data range from roughly 0.5×10^5 through 2.0×10^6 (see May 1975). The Thwaites method was used with a Reynolds number of 1.0×10^5 to be representative of the data. (Note that for the Thwaites method, $C_f \propto \mathrm{Re}^{-1/2}$.) The agreement of the predictions with the data is excellent. The inviscid prediction bounds the data

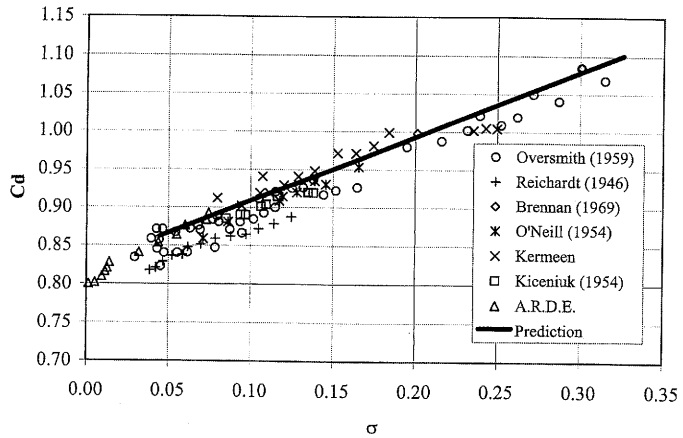

Fig. 14 Comparison of predicted and experimental drag coefficients for a disk cavitator for $4 \leq l_{cav}/d \leq 40$ (data from May 1975)

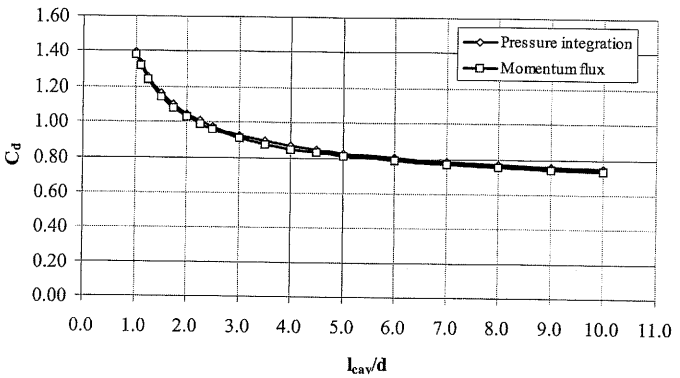

Fig. 15 Comparison of drag coefficients for a disk cavitator predicted by pressure integration and momentum flux, $l_{jet}/d = 50\%l_{cav}/d$

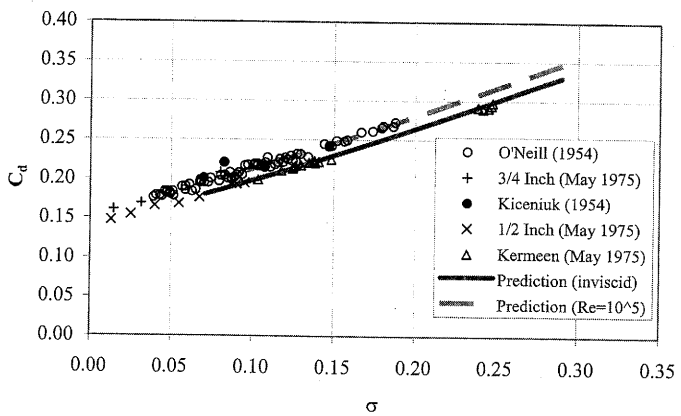

Fig. 16 Comparison of predicted and experimental drag coefficients for a 15 deg half-angle cone cavitator, $2 \leq l_{cav}/d \leq 10$ (data from May 1975)

from below, while the viscid prediction runs through the center of the data. Thus, for cones of small half-angle, it is important to include the skin friction contribution to the cavitator drag. It should be noted that it can be shown that the favorable pressure gradient over a disk cavitator will prevent the transition of the

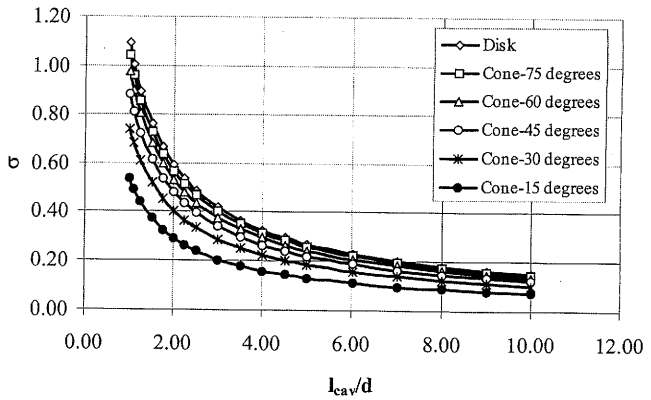

Fig. 17 Cavitation number versus cavity length for conical cavitators

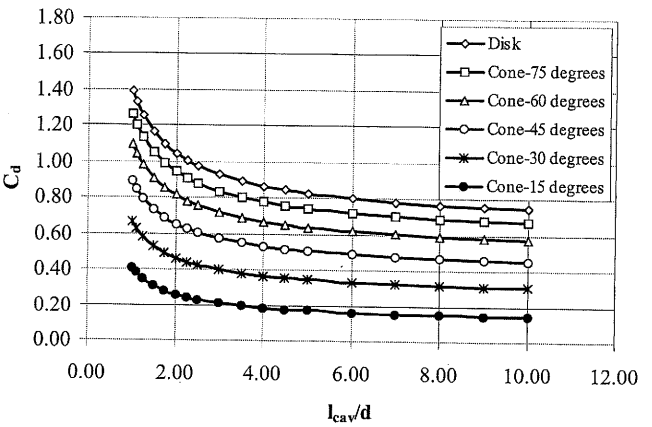

Fig. 18 Drag coefficient versus cavity length for conical cavitators (inviscid)

boundary layer to turbulence. However, for sufficiently small cone angles and sufficiently high Reynolds numbers, transition will occur and the assumption of a laminar boundary layer, as employed here, will need to be modified.

The predicted dependence of cavitation number and drag coefficient on cone half-angle is presented in Figs. 17 and 18, respectively. The variation in cavitation number with cone half-angle is weak at large half-angles, but becomes increasingly important as the half-angle gets smaller. The dependence of the drag coefficient on cone half-angle is strong at all half-angles, but again becomes increasingly important as the half-angle decreases. Note that these results are for the inviscid case. Inclusion of the viscous component of the drag would tend to lessen the importance of cone half-angle since the added viscous drag would increase as the half-angle decreases.

7. Conclusions

As is evident from the results presented in this paper, the predictions of the reentrant jet model are in good agreement with the available experimental results and are consistent with momentum flux requirements. Although the predictions of the older Riabouchinsky-type cavity closure vary only slightly from those of the reentrant jet cavity closure, the reentrant jet model repre-

sents an improvement over the Riabouchinsky-type cavity closure model since the only boundary conditions that need be employed are the physical ones of constant pressure and no flux. Thus, the reentrant jet cavity closure model is a more physically based model.

Acknowledgments

This work was supported by Dr. Kam Ng of the Office of Naval Research (ONR) under the auspices of the High Speed Weapons program and Dr. Stuart Dickinson through the Naval Undersea Warfare Center (NUWC) In-Laboratory Independent Research (ILIR) program.

References

ARDE. (Data obtained from May 1975, but reference not found in May 1975).

ARMSTRONG, A. H. 1954 *Drag Coefficients of Wedges and Cones in Cavity Flow,* ARE Report 21/54. (Data obtained from May 1975).

BRENNEN, C. 1969 A numerical solution of axisymmetric cavity flows, *Journal of Fluid Mechanics,* **37,** 4, 671–688.

CHOU, Y. S. 1974 Axisymmetric cavity flows past slender bodies of revolution, *Journal of Hydronautics,* **8,** 1, 13–18.

DANG, J., AND KUIPER, G. 1999a Re-entrant jet modeling of partial cavity flow on two-dimensional hydrofoils, *Journal of Fluids Engineering,* **121,** 773–780.

DANG, J., AND KUIPER, G. 1999b Re-entrant jet modeling of partial cavity flow on three-dimensional hydrofoils, *Journal of Fluids Engineering,* **121,** 781–787.

DAWSON, V. C. D., AND SEIGEL, A. E. 1970 *The Steady-State Drag Coefficients of Various Cavitating Head Forms,* NOLTR 70-206. (Data obtained from May 1975.)

EFROS, A. G. 1946 Hydrodynamic theory of two-dimensional flow with cavitation, *Dokl. Acad. Nauk. SSSR,* **51,** 267–270.

EISENBERG, P., AND POND, H. L. 1948 *Water Tunnel Investigations of Steady State Cavities,* DTMB Report 668. (Data obtained from May 1975.)

FINE, N. E. 1992 *Nonlinear Analysis of Cavitating Propellers in Nonuniform Flow,* Ph.D. thesis, Massachusetts Institute of Technology, Cambridge, MA.

FINE, N. E., AND KINNAS, S. A. 1993 A boundary element method for the analysis of the flow around 3-D cavitating hydrofoils, JOURNAL OF SHIP RESEARCH, **37,** 1, 213–224.

GILBARG, D., AND SERRIN, J. 1950 Free boundaries and jets in the theory of cavitation, *Journal of Mathematics and Physics,* **29,** 1–12.

GILBARG, D. 1960 *Jets and Cavities,* Handbuch der Physik, vol. 9, Springer-Verlag, Berlin, Germany.

GUERST, J. A. 1959 Linearized theory for partially cavitated hydrofoils, *International Shipbuilding Progress,* **6,** 60, 369–384.

GUERST, J. A. 1960 Linearized theory for fully cavitated hydrofoils, *International Shipbuilding Progress,* **7,** 65, 17–27.

KERMEEN, R. W. (Data obtained from May 1975, but reference not found in May 1975.)

KICENIUK, T. 1954 *An Experimental Study of the Hydrodynamic Forces Acting on a Family of Cavity-Producing Conical Bodies of Revolution Inclined to the Flow,* CIT Hyd. Report E-12.17. (Data obtained from May 1975.)

KINNAS, S. A., AND FINE, N. E. 1990 Non-linear analysis of the flow around partially or super-cavitating hydrofoils by a potential based panel method, *Proceedings,* IABEM-90 Symposium of the International Association for Boundary Element Methods, October, Rome, Italy.

KINNAS, S. A., AND FINE, N. E. 1993 A numerical non-linear analysis of the flow around 2-D and 3-D partially cavitating hydrofoils, *Journal of Fluid Mechanics,* **254,** 151–181.

KLOSE, J., AND ACOSTA, A. J. 1965 Some new measurements on the drag of cavitating disks, JOURNAL OF SHIP RESEARCH, **9,** 102–104. (Data obtained from May 1975.)

KRISHNASWARMY, P., ANDERSON, P., AND KINNAS, S. A. 2001 Re-entrant jet modeling for partially cavitating two-dimensional hydrofoils, *Proceedings,* International Symposium on Cavitation, June 20–23, Pasadena, CA.

LEEHEY, P. 1973 Supercavitating hydrofoils of finite span, *Proceedings of the IUTAM Symposium on Non-steady Flow of Water at High Speeds,* NAUKA Publishing, Moscow.

MAY, A. 1975 *Water Entry and the Cavity-Running Behavior of Missiles,* SEAHAC TR 75-2, Naval Sea Systems Command, Arlington, VA.

O'NEILL, J. P. 1954 *Flow Around Bodies with Attached Open Cavities,* CIT Hyd. Report E-24.7. (Data obtained from May 1975.)

OVERSMITH, R. H. 1959 *Some Observations on Cavitating Flows,* Convair Engineering Department Report ZR-659-015. (Data obtained from May 1975.)

PELLONE, C., AND ROWE, A. 1981 Supercavitating hydrofoils in non-linear theory, *Proceedings,* 3rd International Conference on Numerical Ship Hydrodynamics, August, Paris, France, Basin d'essais des Carenes.

REICHARDT, H. 1946 The Laws of Cavitation Bubbles at Axially Symmetric Bodies in a Flow, M.A.P. Volkenrode Ref: MAP-VG, Reports and Translations No. 766 ONR. (Data obtained from May 1975.)

TULIN, M. P. 1953 *Steady Two-Dimensional Cavity Flows About Slender Bodies,* DTMB Report 834, Navy Department, Washington, DC.

TULIN, M. P. 1964 Supercavitating flows—small perturbation theory, JOURNAL OF SHIP RESEARCH, **7,** 3, 16–37.

UHLMAN, J. S. 1978 A partially cavitated hydrofoil of finite span, *Journal of Fluids Engineering,* **100,** 3, 353–354.

UHLMAN, J. S. 1983 *The Surface Singularity Method Applied to Partially Cavitating Hydrofoils,* Ph.D. thesis, Massachusetts Institute of Technology, Cambridge, MA.

UHLMAN, J. S. 1987 The surface singularity method applied to partially cavitating hydrofoils, JOURNAL OF SHIP RESEARCH, **31,** 2, 107–124.

UHLMAN, J. S. 1989 The surface singularity or boundary integral method applied to supercavitating hydrofoils, JOURNAL OF SHIP RESEARCH, **33,** 1, 16–20.

UHLMAN, J. S., VARGHESE, A. N., AND KIRSCHNER, I. N. 1998 Boundary element modeling of axisymmetric supercavitating bodies, *Proceedings,* 1st HHTC CFD Conference, Naval Surface Warfare Center, Carderock Division, Carderock, MD.

WHITE, F. M. 1974 *Viscous Fluid Flow,* McGraw-Hill, New York.

Appendix A

Axisymmetric Green functions

The expressions for the piecewise constant source and normal dipole potentials take the form

$$G(x,r;\xi,\rho)=\int_{-\pi}^{+\pi}\frac{\rho\,d\varphi}{\sqrt{(x-\xi)^2+r^2+\rho^2-2r\,\rho\cos(\varphi)}} \tag{20}$$

and

$$\frac{\partial G}{\partial n}(x,r;\xi,\rho)=\int_{-\pi}^{+\pi}\frac{\partial}{\partial n}\left\{\frac{1}{\sqrt{(x-\xi)^2+r^2+\rho^2-2r\,\rho\cos(\varphi)}}\right\}\rho\,d\varphi$$

$$=\int_{-\pi}^{+\pi}\left\{n_\xi\frac{\partial G}{\partial\xi}+n_\rho\frac{\partial G}{\partial\rho}\right\}\rho\,d\varphi \tag{21}$$

where

$$\frac{\partial G}{\partial\xi}=\int_{-\pi}^{+\pi}\frac{\rho(x-\xi)}{\left[(x-\xi)^2+r^2+\rho^2-2r\,\rho\cos(\varphi)\right]^{3/2}}d\varphi$$

$$\frac{\partial G}{\partial\rho}=\int_{-\pi}^{+\pi}\frac{-\rho(\rho-r\cos(\varphi))}{\left[(x-\xi)^2+r^2+\rho^2-2r\,\rho\cos(\varphi)\right]^{3/2}}d\varphi \tag{22}$$

Using the integrals defined in Appendix B, we find that

$$G = \rho J_1^0(A,B)$$

$$\frac{\partial G}{\partial \xi} = \rho(x-\xi) J_3^0(A,B) \tag{23}$$

$$\frac{\partial G}{\partial \rho} = -\rho^2 J_3^0(A,B) + \rho r J_3^1(A,B)$$

where

$$A = r^2 + \rho^2 + (z-\zeta)^2$$

$$B = 2r\rho \tag{24}$$

The influence of an axisymmetric panel on itself is determined by noting that for a closed body

$$\iint_{S_i} \frac{\partial G}{\partial n} dS = 2\pi - \sum_{j \neq i} \iint_{S_j} \frac{\partial G}{\partial n} dS \tag{25}$$

for a field point on the body surface.

Appendix B

Evaluation of integrals

The integrals necessary for the evaluation of the axisymmetric Green functions take the general form

$$J_n^m(A,B) = \int_0^{2\pi} \frac{\cos^m(\varphi)}{[A - B\cos(\varphi)]^{n/2}} d\varphi \tag{26}$$

It can then be shown that

$$J_1^0(A,B) = \frac{4}{\sqrt{A+B}} K(k)$$

$$J_3^0(A,B) = \frac{4}{(A-B)\sqrt{A+B}} E(k) \tag{27}$$

where $E(k)$ and $K(k)$ are elliptic integrals defined by

$$K(k) = \int_0^{\pi/2} \frac{d\varphi}{\sqrt{1 - k^2 \sin^2(\varphi)}}$$

$$E(k) = \int_0^{\pi/2} \sqrt{1 - k^2 \sin^2(\varphi)}\, d\varphi \tag{28}$$

and

$$k^2 = \frac{2B}{A+B} \tag{29}$$

Equation (26) may be used to derive the recursion relation

$$J_n^m(A,B) = \frac{1}{B}\left[A J_n^{m-1}(A,B) - J_{n-2}^{m-1}(A,B)\right] \tag{30}$$

which may be employed to determine the other required integrals in terms of J_1^0 and J_3^0.

Appendix C

Mass and momentum control volume analyses

The control volume for this analysis with the associated boundary designations is depicted in Fig. 19.

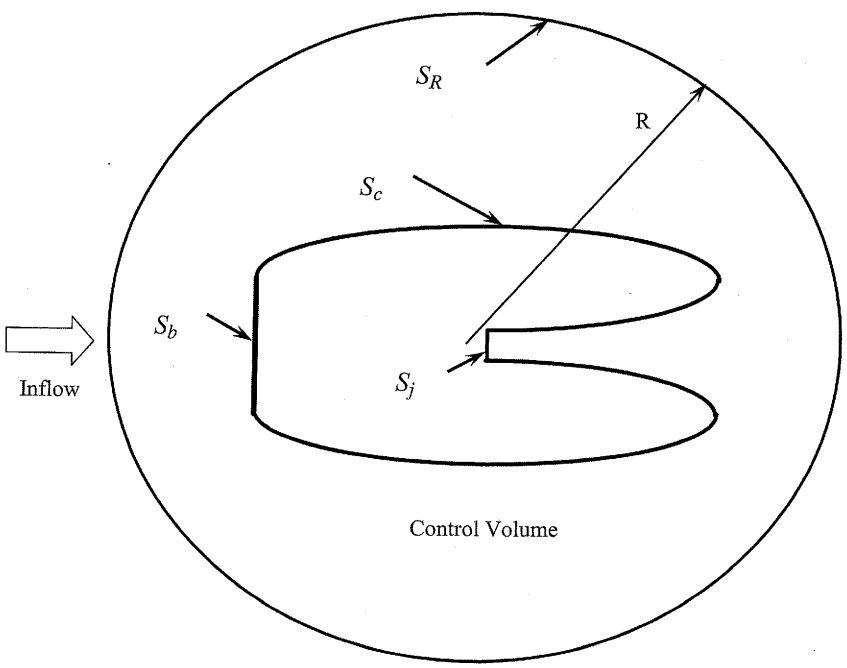

Fig. 19 Control volume with boundary designations

Employing this control volume plus the surface at infinity, S_∞ (where $S_\infty = \lim_{R\to\infty} S_R$ and S_R is the surface at radius R), we may perform a control volume analysis of the conservation of mass using

$$\iint_{\substack{S_b+S_c\\+S_j+S_\infty}} \rho(n_j u_j)\, dS = 0 \tag{31}$$

Assuming, for large r, that the total potential may be approximated as

$$\Phi \approx U_\infty x - \frac{Q}{4\pi r} + O\left(\frac{1}{r^2}\right) \tag{32}$$

where Q is the source strength seen in the far field, we find that the contributions to equation (31) then become

$$\iint_{S_b} \rho(n_j u_j)\, dS = 0$$

$$\iint_{S_c} \rho(n_j u_j)\, dS = 0$$

$$\iint_{S_j} \rho\,(n_j u_j)\, dS = \rho U_{jet} \frac{\pi}{4} d_{jet}^2$$

$$\iint_{S_\infty} \rho\,(n_j u_j)\, dS = \rho Q \tag{33}$$

where $U_{jet} = U_\infty \sqrt{1+\sigma}$. Hence, we find that

$$Q = -\frac{\pi}{4} d_{jet}^2 U_{jet} \tag{34}$$

Performing the momentum analysis using

$$\iint_{\substack{S_b+S_c\\+S_j+S_\infty}} \rho u_i (n_j u_j)\, dS + \iint_{\substack{S_b+S_c\\+S_j+S_\infty}} n_i (p - p_c)\, dS = 0 \tag{35}$$

then yields the integrals

$$\iint_{S_b} \rho u (n_j u_j)\, dS = 0$$

$$\iint_{S_c} \rho u (n_j u_j)\, dS = 0$$

$$\iint_{S_j} \rho u (n_j u_j)\, dS = -\rho U_{jet}^2 \frac{\pi}{4} d_{jet}^2$$

$$\iint_{S_\infty} \rho u (n_j u_j)\, dS = \frac{4}{3} \rho Q U_\infty \tag{36}$$

and

$$\iint_{S_b} n_x (p - p_c)\, dS = D$$

$$\iint_{S_c} n_x (p - p_c)\, dS = 0$$

$$\iint_{S_j} n_x (p - p_c)\, dS = 0$$

$$\iint_{S_\infty} n_x (p - p_c)\, dS = -\frac{1}{3} \rho Q U_\infty \tag{37}$$

so that

$$D = \frac{\pi}{4} \rho d_{jet}^2 U_{jet}^2 - \rho U_\infty Q \tag{38}$$

or, in dimensionless form

$$C_d = \frac{\pi}{2} \left(\frac{d_{jet}}{d}\right)^2 (1+\sigma) \left[1 + \frac{1}{\sqrt{1+\sigma}}\right] \tag{39}$$

where we note that $d_{jet} = d_{jet}(\sigma)$.